Available online at www.sciencedirect.com

ScienceDirect

Geochimica et Cosmochimica Acta 200 (2017) 280–294

Geochimica et Cosmochimica Acta

www.elsevier.com/locate/gca

Effects of shock and Martian alteration on Tissint hydrogen isotope ratios and water content

L.J. Hallis [a,b,e,*], G.R. Huss [a,b], K. Nagashima [b], G.J. Taylor [a,b], D. Stöffler [c], C.L. Smith [d], M.R. Lee [e]

[a] NASA Astrobiology Institute, Institute for Astronomy, University of Hawai'i, 2680 Woodlawn Drive, Honolulu, HI 96822-1839, United States
[b] Hawai'i Institute of Geophysics and Planetology, Pacific Ocean Science and Technology (POST) Building, University of Hawai'i, 1680 East-West Road, Honolulu, HI 96822, United States
[c] Museum of Natural History, Invalidenstrasse 43 Leibniz-Institut Für Evolutions-Und Biodiversitätsforschung, 10115 Berlin, Germany
[d] Department of Earth Sciences, The Natural History Museum, Cromwell Road, London SW7 5BD, UK
[e] School of Geographical and Earth Science, University of Glasgow, Gregory Building, Lillybank Gardens, Glasgow G12 8QQ, Scotland, UK

Received 30 November 2015; accepted in revised form 24 December 2016; available online 3 January 2017

Abstract

The Tissint meteorite, a picritic shergottite, fell to Earth in Morocco on the 18th of July 2011, and is only the fifth Martian meteorite witnessed to fall. Hydrogen isotope ratios and water contents are variable within different minerals in Tissint. Ringwoodite and shock melt pockets contain elevated D/H ratios relative to terrestrial values ($\delta D = 761–4224‰$). These high ratios in recrystallized phases indicate significant implantation of hydrogen from the D-rich Martian atmosphere during shock. In contrast, although olivine has detectable water abundances (230–485 ppm), it exhibits much lower D/H ratios ($\delta D = +88$ to $-150‰$), suggesting this water was not implanted from the Martian atmosphere. The minimal terrestrial weathering experienced by Tissint gives confidence that the olivine-hosted water has a Martian origin, but its high concentration indicates direct inheritance from the parental melt is improbable, especially given the low pressure of olivine crystallisation. Incorporation of a low δD crustal fluid, or deuteric alteration during crystallisation, could explain the relatively high water contents and low D/H ratios in Tissint olivine.

Keywords: Martian meteorites; Shock; Hydrogen isotopes

1. INTRODUCTION

1.1. Tissint mineralogy, petrology and shock history

Tissint fell to Earth in Morocco on the 18th of July 2011, and is only the fifth Martian meteorite witnessed to fall. Mineralogical and petrological investigations indicate that Tissint is a picritic shergottite, with a composition similar to lithologies A and C of EETA 79001 (Chennaoui Aoudjehane et al., 2012). The interior of the meteorite consists of olivine macrocrysts set in a fine-grained matrix of pyroxene, diaplectic plagioclase glass (maskelynite) and smaller olivine phenocrysts (Irving et al., 2012). The olivine phenocrysts have lower Fo# at the core of each grain than the larger olivine macrocrysts ($Fo_{70–76}$ vs. $Fo_{>80}$, where $Fo\# = (Mg/(Fe + Mg)) * 100$) (Balta et al., 2015). The matrix is highly fractured and contains numerous dark shock veins and patches filled with a black glassy material that encloses bubbles (e.g., Chennaoui Aoudjehane et al., 2012; Smith and Ahmed, 2012; Baziotis et al., 2013; Chen et al., 2015). Water-rich

* Corresponding author at: University of Glasgow, School of Geographical and Earth Sciences, Room 514 Gregory Building, Lillybank Gardens, Glasgow G12 8QQ, UK.
E-mail address: lydia.hallis@glasgow.ac.uk (L.J. Hallis).

http://dx.doi.org/10.1016/j.gca.2016.12.035
0016-7037/

amphibole has been reported in Tissint pigeonite-hosted melt inclusions (Williams et al., 2014).

The similarity between the whole-rock REE pattern of Tissint and the depleted shergottites (Irving et al., 2012), and the fact that its cosmic ray exposure age matches that of the olivine-phyric shergottites (Nishiizumi et al., 2012), indicate Tissint was ejected from Mars along with these shergottites. However, Tissint's crystallisation age of 574 ± 20 Ma (Brennecka et al., 2014) is older than most of the other shergottites (165–475 Ma, e.g., Nyquist et al., 2001), implying it originated from an older lithology at the shergottite launch site – only Dhofar 019 has a similar age to Tissint (Borg et al., 2001).

Because Tissint was seen to fall, it has been minimally terrestrially contaminated. The stones fell in an exceptionally dry desert environment (Chennaoui Aoudjehane et al., 2012). None of the samples at the London Natural History Museum have terrestrial mud or soil adhering to the fusion crust or present within surface cracks, suggesting the dusty desert environment remained dry during the short residence of the stones (<4 months). An extensive study of Tissint sulphides noted the complete lack of the sulphide alteration produced during terrestrial weathering (e.g., Fe-oxyhydroxides) (Gattacceca et al., 2013). In addition, the recent nature of the fall means the stones have been exposed to the terrestrial atmosphere for a very short period of time - other Martian meteorite falls have been stored in atmospheric conditions for decades, if not centuries (e.g., Nakhla fell in 1911, Shergotty in 1865, and Chassigny in 1815). In this sense Tissint is ideal for studying the abundance and hydrogen isotope (D/H) ratios of Martian water. However, the effects of shock potentially add an additional complication to understanding water in this meteorite.

The shock history of Tissint has been widely studied. High pressure phases such as ringwoodite, vitrified perovskite, akimotoite, majorite, lingunite, tuite, stishovite and magnesiowüstite have been observed (Baziotis et al., 2013; Hu et al., 2013; Summerson et al., 2013; Sharp et al., 2014), as well as two new high pressure minerals – tissintite and ahrensite (Ma et al., 2015). In addition, deformational features are common, such as planar fractures and mosaicism in olivine, mechanical twinning in pyroxene, and the conversion of plagioclase to diaplectic glass or 'normal' plagioclase glass (distinguished by the presence of flow lines and vesicles in the latter). Baziotis et al. (2013) suggested that a very large impact produced the high pressure and temperature phases in Tissint, from which the authors derive pressure and temperature values of ~25 GPa and 2000 °C, respectively. However, another theory involving a shorter duration of shock, which eliminates the necessity for a large impact event, has also been proposed (e.g., Hu et al., 2013; Sharp et al., 2014; Walton et al., 2014). The latter theory explains the apparent shock heterogeneity in Tissint by a relatively short duration shock pulse combined with a complex thermal history. Relatively slow cooling of hot post-shock regions of the rock that were adjacent to large shock melt areas likely transformed high-pressure phases back to their low-pressure polymorphs. In contrast, smaller melt veins would have cooled faster, thus better preserving their high shock pressure phases. As an added complication, Tissint's paleomagnetic record suggests that after this major shock event the rock cooled on the surface of Mars, i.e. this event was not that which launched Tissint from the Martian surface (Gattacceca et al., 2013).

1.2. The effect of shock on mineral water contents and D/H ratios

A number of experimental studies have shown that gases (noble gases, CO_2, N_2) can be implanted into mineral defects (dislocations, point defects, cracks and pores) and melt veins/pockets during shock (Bogard et al., 1986, 1989; Wiens and Pepin, 1988). This process is not mineral specific, and can potentially introduce hydrogen into nominally anhydrous minerals. No isotopic fractionation was reported for the implanted noble gases, CO_2 and N_2, but the large mass difference between the two hydrogen isotopes (^{1}H and ^{2}H/D) could potentially cause fractionation. Gases trapped in both defects and melt pockets/veins can persist even at the high temperatures used in laboratory extraction (>600 °C; Bogard et al., 1986).

On Mars there is a large difference in D/H ratio between the atmosphere and the planetary interior. The D/H ratio of the Martian interior, measured via hydrous minerals in Martian meteorites, appears to be similar to that of terrestrial rocks and Vienna Standard Mean Ocean Water (VSMOW) (Usui et al., 2012; Hallis et al., 2012b). In contrast, because of the preferential loss of the lighter hydrogen isotope to space via Jeans (thermal) escape (Donahue, 1995), as well as increased non-thermal escape after the cessation of Mars' dynamo, the Martian atmosphere is currently five times enriched in deuterium compared to VSMOW (Bjoraker et al., 1989; Webster et al., 2013). The Martian cryosphere (e.g., subsurface ice) is also reported to have a high D/H ratio (Usui et al., 2015). Therefore, any incorporation of atmospheric hydrogen into minerals or glasses at the Martian surface would result in an increase in their D/H ratio. This effect has been measured in Martian amphibole (e.g., Giesting et al., 2015).

1.3. Aim

Measurements of the water content and D/H ratios of specific constituents of Martian meteorites are currently used to determine the presence of separate water reservoirs on Mars. However, the effect of impact induced shock on the D/H ratio and water content of individual minerals is still not fully understood. Tissint nominally anhydrous minerals have previously been reported to contain detectable water (e.g., Tucker et al., 2015; Mane et al., 2016). Therefore, we measured the D/H ratios and water contents of primary igneous phases (olivine, pyroxene, plagioclase (now maskelynite), and melt inclusions in Tissint, as well as shock-produced phases (ringwoodite and shock melt pockets), with the aim of determining how shock affects hydrogen in different minerals. We subsequently analysed olivine and ringwoodite at sub-micron scales to determine exactly how hydrogen was fixed into these minerals.

2. METHODOLOGY

2.1. Sample preparation

Tissint thin-sections MfN S1 and MfN S2 were analysed for shock characteristics (e.g., mosaicism, fracturing, presence of shock produced glass) at the Berlin Museum of Natural History, using optical microscopy (Supplementary materials 1). The samples analysed with the ion-microprobe and transmission electron microscope included a thick slice of Tissint from the Natural History Museum, London (P18494, from BM.2012,M3) along with a 100.94 mg sample (also from BM2012,M3) made up of polymineralic clasts. A large (~2 mm diameter) olivine macrocryst containing what appeared to be a shocked melt pocket was selected from the latter sample and embedded into indium metal set in a steel bullet (named BM2012, M3_1). As indium is easily malleable, it was formed and shaped around the grain to hold it in place during polishing. Polishing was performed without the use of water for both BM2012,M3_1 and P18494 (methanol was used for both). Indium mounted BM2012,M3_1 served as a control sample, as P18494 was epoxy mounted – although visible epoxy-filled cracks were avoided during ion-microprobe analyses, a non-epoxy-mounted sample served as a useful comparison to the P18494 data.

Preparation methods and storage conditions are important for samples intended for hydrogen isotopic analyses. Terrestrial hydrogen contamination can occur during sample cutting, polishing and cleaning, as well as during subsequent atmospheric exposure (e.g., Boctor et al., 2003; Hallis et al., 2012a). To avoid these issues as far as possible each sample was placed in a vacuum oven at 60 °C for 1 week prior to carbon coating, and returned to the oven directly after coating. This temperature is high enough to remove adsorbed water from the sample surface, but not high enough to remove structurally bound hydrogen from the target phases (Hallis et al., 2012a).

2.2. Sample imaging and mineralogical classification of areas of interest

Samples P18494 and BM2012, M3_1 were imaged using the JEOL JSM-5900LV scanning electron microscope at the University of Hawai'i. Backscatter and secondary electron images were produced for navigation. X-ray images and EDX spectral data were used to select areas of interest. Areas of interest were selected based on the presence of shock melt pockets hosted within different minerals (Fig. 1). High-resolution images (1–3 μm pixel sizes) of each area of interest were used to assess the potential for contamination. For example, secondary electron images show whether an area is clean of detritus and whether the carbon coating is even. High-resolution images also highlight the presence of cracks or voids that need to be avoided during ion-microprobe analysis. Areas of interest were also imaged after ion-microprobe analysis to verify the positions of the sputtered regions (Supplementary materials 2).

Following secondary-ion mass spectrometry (see Section 2.3), Raman spectrometry was employed to further determine the mineralogy of the areas of interest. A Renishaw inVia Raman microscope at the University of Glasgow was operated with a 514 nm laser, and a spot size of ~1 μm. Laser focusing on the sample was performed through a petrographic microscope equipped with a 100× objective. The spectra were accumulated in 5 increments with an exposure time of 5 s each, using 25 mW laser power. Calibration was made with respect to wave number using a silicon standard. The collected Raman spectra were processed (curve fitted to determine the peak positions) using the Renishaw WIRE software.

2.3. Hydrogen isotope measurements via secondary-ion mass spectrometry (SIMS)

For detailed SIMS methods see Supplementary materials 2. Deuterium and hydrogen isotopic compositions were analysed *in situ* with the UH Cameca ims 1280 ion microprobe, following the protocol of Hallis et al. (2012a). Two basaltic glass standards (GL07 D51-3 and GL07 D52-5) were used to correct for instrumental mass fractionation (IMF). The water abundances for our specific chips of D51-3 and D52-1 were measured using FTIR by Rhea Workman, the D/H values of these standards were previously determined by Hauri (2002) and Hauri et al. (2006). GL07 D51-3 contains 0.469 wt.% H_2O and has a δD value of −52‰, GL07 D52-5 contains 1.086 wt.% H_2O and has a δD value of −51‰. Based on standard measurements a calibration line can be produced to estimate the water content of each unknown (Supplementary materials 2). Aubaud et al. (2007) reported matrix affects between olivine and basaltic glasses could be as much as a factor of 2.79, as the olivine sensitivity factor is lower than that of basalt glass, leading to lower inferred H abundances. Therefore, we provide minimum olivine water contents for Tissint in Table 1, based on this sensitivity factor (see Supplementary materials 2 for details). It is important to note that these are minimum values, as in reality the matrix affect for each analysis may not be as large as the maximum possible between olivine and basaltic glass. The H_2O detection limit for each analytical run is estimated via the $^{1}H/^{30}Si$ ratio in an anhydrous San Carlos olivine standard – Mosenfelder et al. (2011) determined that San Carlos olivine contains 0–0.3 ppm H_2O. Based on San Carlos olivine measurements the instrumental detection limit was 106 ppm and 225 ppm H_2O during the July and October analytical runs, respectively. Any sample measurements falling below or around the detection limit were not deemed reliable.

2.4. Focused-ion-beam section preparation and transmission–electron-microscope analysis

To allow transmission–electron-microscope (TEM) analysis, three electron-transparent focused-ion-beam (FIB) sections were cut from the surface of the indium mounted BM.2012, M3_1. The sections were prepared

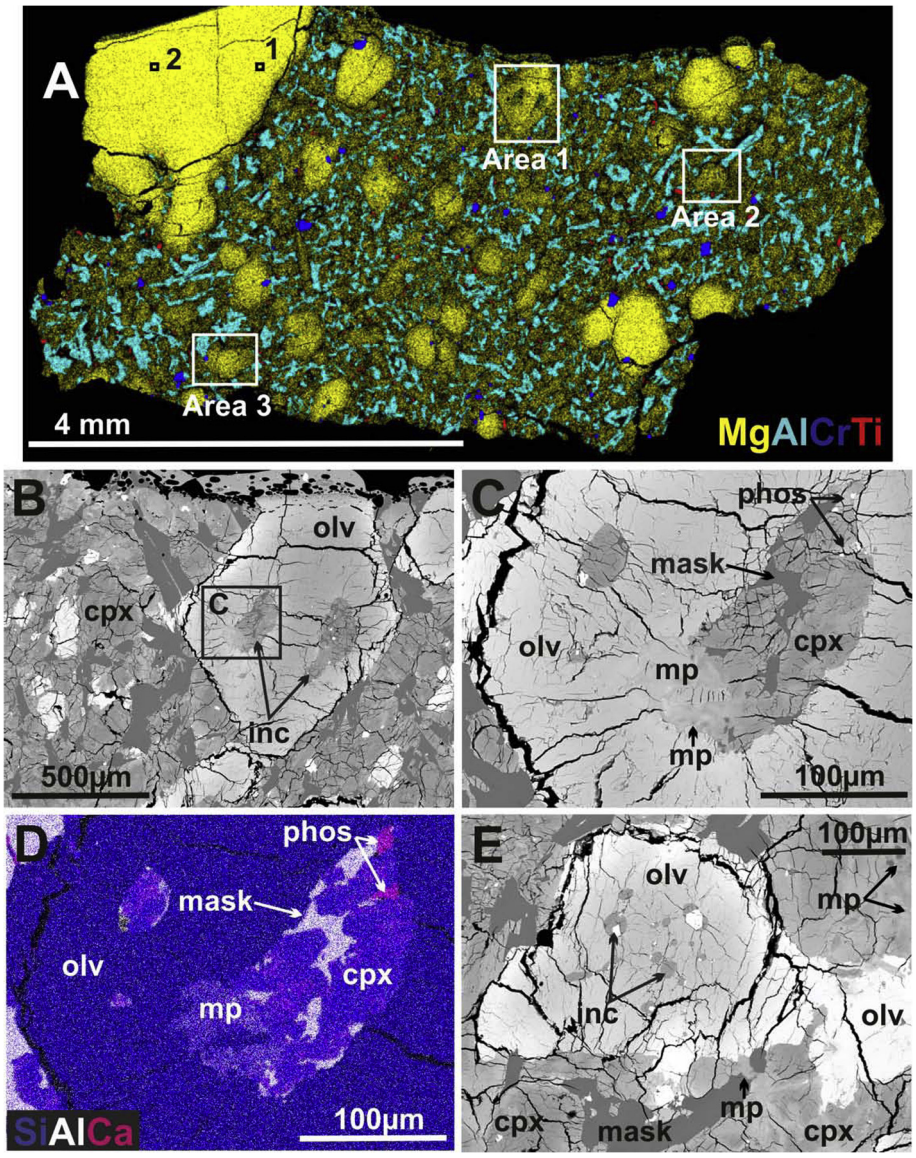

Fig. 1. X-ray (A, D) and backscatter electron (B, C, E) images of Tissint sample P18494. Areas 1 and 2 are shown in more detail in images B–D and E, respectively. Colour codes for X-ray images are shown as coloured text for each element (e.g., Mg = yellow in A). Tissint contains olivine (olv) macrocrysts and phenocrysts (yellow in A), the latter of which commonly contain melt inclusions (Inc.) consisting of clinopyroxene (cpx), maskelynite (mask), phosphate (phos) and metal oxides (bright areas in E melt inclusions). Melt pockets (mp) are commonly hosted within olivine (C, D), but can also be unassociated with olivine (E).

using a FEI Duomill dual-beam FIB instrument operated with a 30 kV Ga+ ion beam and following the procedure of Lee et al. (2003). Prior to milling the area of interest was capped with a 15 µm long by 4 µm wide and 0.1 µm thick layer of Pt that was applied using a gas injection system and deposited by interaction with the electron beam. Initially, each foil was ion milled to a thickness of approximately 1 µm using high (~1 nA) beam currents. Following its *in situ* extraction the thick foil was welded to the tines of a copper holder using electron- and ion-beam-deposited Pt and reduced to approximately 100 nm thickness at lower current (~100 pA).

Bright- and dark-field diffraction-contrast images and selected area electron diffraction (SAED) patterns were acquired from the FIB-sections using a FEI T20 TEM operated at 200 kV. FIB-section 3 was further studied by bright-field and high-angle annular dark-field (HAADF) scanning TEM (STEM) imaging using a JEOL ARM200cF MagTEM operated at 200 kV. The microscope is equipped with a Gatan Quantum electron spectrometer for major- and minor-element quantitative energy-dispersive X-ray (EDX) analysis. EDX conditions included a 0.4–0.6 nm spot size and 100 pA current on the sample, at 20 keV with a 40 µm condenser aperture. The count time for each anal-

ysis was 30 s. X-ray spectra were quantified via a standardless procedure using Cliff–Lorimer correction.

3. RESULTS

3.1. Shock metamorphism

The primary igneous texture of the coarse-grained Tissint olivine basalt is essentially preserved in most parts of thin-sections MfN S1 and MfN S2, although plagioclase has been completely transformed to diaplectic glass (maskelynite) (Supplementary materials 1). Local melt pockets extending occasionally into melt veins are present, but generally affect only small regions (~5–10 grains) of plagioclase, pyroxene and olivine. In these regions brownish melt (dominated by the mafic minerals) and vesiculated plagioclase glass has developed. Olivine outside the melt pockets shows strong mosaicism and planar fractures, indicating the highest degree of shock before solid state recrystallisation and melting. In rare cases, olivine-hosted fractures are filled with deposits of sulphide and metal – a process known as shock blackening (see also Baziotis et al., 2013; Summerson et al., 2013). Inside melt pockets, olivine is affected by solid state recrystallisation, or is rounded due to partial melting and is finely recrystallised. Plagioclase glass within or near the melt regions shows small vesicles and minor flow textures. Clinopyroxene displays shock-induced mosaicism and mechanical twinning.

3.2. Mineralogy of specific areas of interest

Areas of interest (AOI) were selected from areas with differing evidence for shock (Fig. 1). Four AOI were selected in sample P18494, including one large olivine macrocryst (~3 mm diameter), and three AOI centred around smaller olivine phenocrysts (<1 mm) (Fig. 1). The large olivine macrocryst contains no melt pockets or mineral/melt inclusions visible via SEM imaging. Two of the smaller olivine phenocrysts (P18494 areas 1 and 2) contain melt inclusions, within which clinopyroxene and plagioclase (now in the form of maskelynite) have crystallised, commonly accompanied by chromite spinel and phosphate. One of the melt inclusions within P18494 area 1 has been shock melted at its edge, along with the adjacent olivine (Fig. 1c and d). Raman spectra of this area show no peaks due to the lack of crystal structure. Two areas of shock-produced melt are visible in area 2, one at a clinopyroxene and maskelynite boundary, and another wholly within a clinopyroxene phenocryst (Fig. 1e). Although magnetite is not visible in the SEM images of P18494 area 1 and 2 melt pockets, magnetite Raman spectra were located in these areas (Fig. 2). In addition, ringwoodite is present within the clinopyroxene-hosted melt glass of area 2. Ringwoodite can be distinguished from olivine by its characteristic Raman peaks at 792 and 843 cm^{-1} (e.g., Koch-Muller et al., 2009) (Fig. 2). P18494 area 3 consists of a clean olivine phenocryst with no inclusions, the D/H ratio of which was measured as a comparison to the inclusion-rich phe-

Table 1
Water content and D/H ratios of various mineral phases in the Tissint Martian meteorite.

	Sample and phase	H_2O (ppm)	2σ(‰)	δD (‰)	2σ (‰)
July 2013 – P18494	Shock melt pocket 1	1677	214	761	46
	Shock melt pocket 2	2088	266	842	47
	Shock melt pocket 3	1711	218	1160	48
	Shock melt pocket 4	336	43	1847	67
	Shock melt pocket 5	376	48	1012	58
	Olivine phenocryst 1	*564	201	−51	46
	Olivine phenocryst 2	1203	428	−149	47
	Olivine phenocryst 3	441	157	−73	49
	Olivine phenocryst 4	866	308	−105	47
	Olivine macrocryst 1	1273	453	−80	46
	Olivine macrocryst 2	967	344	−78	47
	Melt inclusion 1	5629	718	372	46
	Melt inclusion 2	4888	623	−95	46
	Melt inclusion 3	5256	670	−98	46
	Clinopyroxene 1	1288	198	−131	47
	Maskelynite 1	216	28	225	65
	SC olivine standard†	106	12	–	–
Sept–Oct 2013 BM2012,M2_1	Ringwoodite 1	769	87	3834	79
	Ringwoodite 2	1132	128	4224	77
	Ringwoodite 3	714	81	3875	81
	Olivine macrocryst 1	230	73	−43	67
	Olivine macrocryst 2	485	153	88	65
	Olivine macrocryst 3	270	85	41	67
	SC olivine standard	224	25	–	–

* Minimum water contents for olivine, based on the possible matrix affects between these crystalline minerals and basaltic glass.
† As San Carlos olivine is anhydrous, the hydrogen detected must be derived from the surface of the standard, and/or hydrogen present in the sample chamber that is not accounted for by the Egun background correction. SC olivine water contents therefore represent the detection limit for each analytical run.

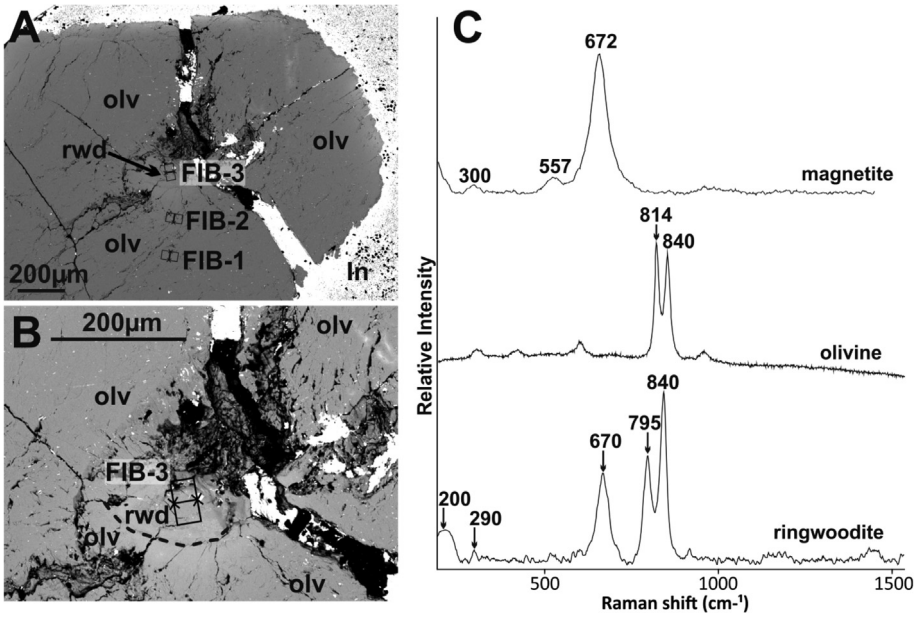

Fig. 2. Backscatter electron images (A, B) of indium (In) mounted sample BM2012,M2_1 with representative Raman spectra (C). The olivine (olv) phenocryst hosts a ~100 µm by 200 µm shocked area mostly consisting of ringwoodite (rwd). The boundary between ringwoodite and the olivine host is approximated by the black dashed line. The location of FIB-sections are shown. Magnetite, olivine and ringwoodite Raman spectra (C) were collected from this sample. Magnetite and ringwoodite, along with glass, were also detected in the melt pockets of P18494 area 2 (Fig. 1e).

nocryst olivine of areas 1 and 2. Sample BM.2012,M3_1 consists of an olivine macrocryst with a central shocked zone containing ringwoodite and magnetite (as shown via Raman spectra), but no melt glass (Fig. 2).

3.3. Hydrogen isotope ratios and water contents

The water content of Tissint olivine macrocrysts and phenocrysts is higher than is typical for terrestrial crustal olivine (230–1273 ppm vs. <200 ppm H_2O (Withers et al., 2011; Manghnani et al., 2013)). There is no difference in water content between the two olivine populations (Table 1; Fig. 3). High olivine water contents in sample P18494 could be partially accounted for by epoxy contamination, as the olivine water contents in indium mounted sample BM.2012,M3_1 do not extend as high as those in P18494 (230–485 ppm vs. 441–1273 ppm H_2O). In addition, there is a weak correlation between decreasing δD values and increasing water contents in P18494 olivine, indicative of terrestrial (epoxy) contamination. However, BM.2012, M3_1 olivine still has a higher water content than typical terrestrial olivine crystallized at low-pressures. The lowest value for BM 2012.M3_1 is close to the detection limit (224 ppm H_2O), but the highest value is more than twice this value. As these are minimum values, having been adjusted for the maximum possible matrix affects (see Section 2.3), it appears that Tissint olivine does contain detectable water, in agreement with the results of Mane et al. (2016) (Fig. 3). All D/H ratios for olivine plot within a δD range of +88 to −149‰ (Table 1; Fig. 3). This range is within error of the δD values in terrestrial rocks and minerals, which commonly vary between −140 and +60‰ (e.g., Shaw et al., 2012 and references therein). This range is also within error of Martian mantle minerals (−78 to +285‰, Usui et al., 2012; Hallis et al., 2012b).

Clinopyroxene in sample P18494 also has a relatively high water content (1552 ppm) and low δD value (−131‰). However, only one measurement of clinopyroxene was made, and this measurement was in an epoxy mounted sample. Therefore, limited significance can be given to this result. Maskelynite contains only 216 ppm H_2O with a δD value slightly higher than olivine or clinopyroxene (+225‰). Maskelynite in Tissint has a much lower density of fractures than olivine and clinopyroxene, hence there is less opportunity for epoxy contamination. Recent studies suggest that Tissint maskelynite contains varying amounts of water (~30–1407 ppm, Tucker et al., 2015; Mane et al., 2016). Our maskelynite falls towards the lower end of this range.

P18494 olivine-phenocryst-hosted melt inclusions contain by far the highest water contents recorded in the present study, at between 4888 and 5629 ppm H_2O. Although some of this water can be accounted for by epoxy contamination in P18494, the water-content variation between melt inclusion analyses and between different phases in P18494 cannot be explained by contamination. Melt inclusion δD values range between −98‰ and 372‰, with the highest value produced from the inclusion with the highest water content (Fig. 3). The water-rich nature of these inclusions in comparison to nominally anhydrous minerals may be expected, as inclusion glass can be hydrous, and melt inclusions within early crystallising

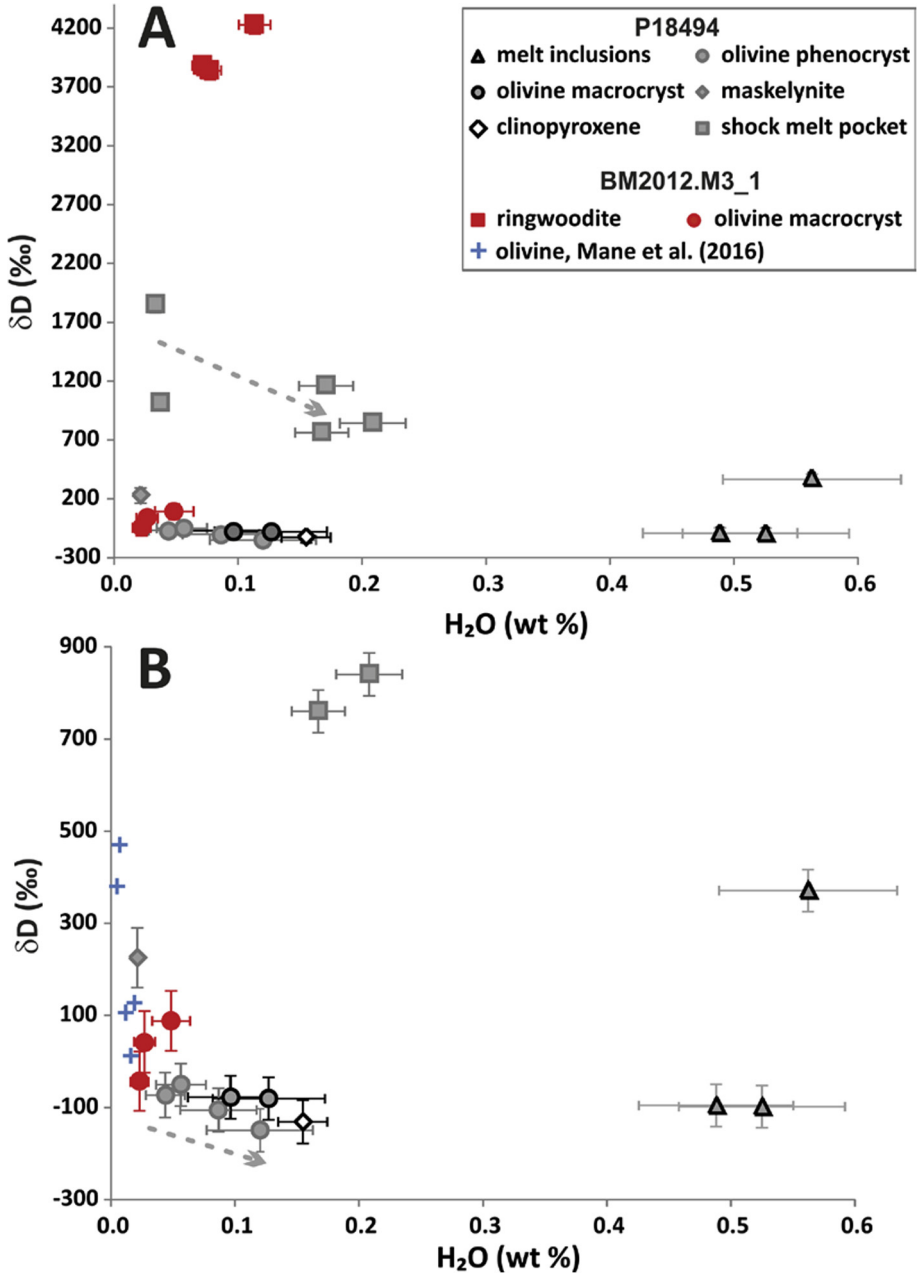

Fig. 3. Plots of δD vs. H_2O for individual phases in Tissint. The grey arrows indicate epoxy resin contamination trends in the olivine and olivine-bound melt pockets of sample P18494. (B) shows a detail of (A) with a smaller scale on the *y*-axis, and the addition of Mane et al. (2016) olivine data from an anhydrously prepared sample. Uncertainties are 2σ.

phases (such as olivine in Tissint) should represent the whole melt composition. However, Tissint melt inclusions are crystalline, generally consisting of clinopyroxene and shock isotropized plagioclase (maskelynite), commonly with Cr-spinel and phosphate (Fig. 1). Therefore, it is difficult to avoid heterogeneities during SIMS data collection from these melt inclusions, which may explain the variation in water content and D/H ratios between the three melt inclusion analyses. In addition, Mane et al. (2016) argued that postcrystallisation processes, such as subsolidus interaction with Martian crustal fluids, or diffusive loss of hydrogen, could produce the measured variations in D/H and H_2O content in Tissint melt inclusions.

Shock melt and ringwoodite show high δD values, although the values in BM.2012,M3_1 are much higher than those in P18494 (3834–4224‰ vs. 761–1847‰, respectively). The water content of P18494 shock melt is spatially highly variable (336–2088 ppm H_2O), and increasing δD with decreasing H_2O could be indicative of degassing during shock, as olivine converts to shocked melt (Fig. 3). This trend is similar to that reported for shocked serpentine (Tyburczy et al., 1990, 2001). However, decreasing δD with

increasing H_2O could also represent increasing amounts of epoxy contamination, and so this trend should be viewed with caution. The water content and δD values of ringwoodite in BM.2012,M3_1 are more tightly clustered and there is a hint of a positive correlation between δD and H_2O.

3.4. Olivine and ringwoodite structure and mineralogy

In an attempt to understand the reasons for high concentrations of H_2O in Tissint olivine, as well as the mineralogy of the highly shocked areas, three focused ion beam (FIB)-sections were cut from sample BM.2012,M3_1. The first FIB-section (FIB-1) was taken from the olivine macrocryst ~200 μm from the ringwoodite, the second FIB-section (FIB-2) was cut from an area of the olivine directly adjacent to ringwoodite, and the third FIB-section (FIB-3) was taken from within the ringwoodite itself (Fig. 2). These FIB-section locations were chosen in order to determine whether olivine and ringwoodite where pure, or contained other phases on a sub-micron scale (e.g., water-bearing alteration phases in olivine).

SAED confirms that FIB-1 and FIB-2 sampled pure olivine, with no associated aqueous alteration or high pressure minerals. In both foils the olivine contains sub-grains and [0 0 1] (0 1 0) screw dislocations (Fig. 4). The dislocation density is 3.64×10^{13} m^{-2} in FIB-1 and 8.63×10^{13} m^{-2} in FIB-2. The higher value for FIB-2 was expected, because it was obtained from closer to the ringwoodite. These densities are slightly lower than that calculated for the Tenham L6 chondrite (2×10^{14} m^{-2}), which is reported to show evidence for heterogeneous shock pressures between 25 and 45 GPa (Langenhorst et al., 1995; Xia et al., 2006).

FIB-3 exhibits a very different texture to FIB-1 and FIB-2. At the edge closest to the boundary with olivine, FIB-3 contains ringwoodite grains up to 2 μm in length, showing typical fibrous habits (Fig. 5). A fragment of olivine is also visible towards this end of the section. Distinct elongated ringwoodite grains gradually give way to a more homogeneous mass of ringwoodite, with 1–3 wt.% Fe, and in at least one location, detectable Ca (Table 2). This ringwoodite contains <0.25 μm diameter spherules that increase in abundance with distance from the boundary with olivine (Fig. 5). Quantitative analyses of these spherules by STEM-EDX show a range extending from olivine/ringwoodite towards $Mg_{0.9}Fe_{0.1}O$ (Fig. 6). These data can be explained by variable degrees of mixing within the analysed volume of olivine/ringwoodite and $Mg_{0.9}$ magnesiowüstite. SAED patterns obtained from the spherules can be indexed as a cubic mineral with an a-axis dimension of ~0.84 nm, whereas $Mg_{0.9}$ magnesiowüstite has an *a*-axis of 0.4229 nm (Marquardt et al., 2009). This apparent doubling of the *a*-axis length can be accounted for as the spherules have a superlattice, as has been observed for nanoparticles of other compounds with a rock salt structure (e.g., Walsh et al., 2013).

The olivine fragment shows good compositional stoichiometry, but ringwoodite contains more Si and Mg and less Fe than olivine, producing non-stoichiometric compositions (Table 2). The presence of Mg-rich magnesiowüstite should mean the ringwoodite is more Fe-rich than olivine. The fact that this correlation is not seen can be explained

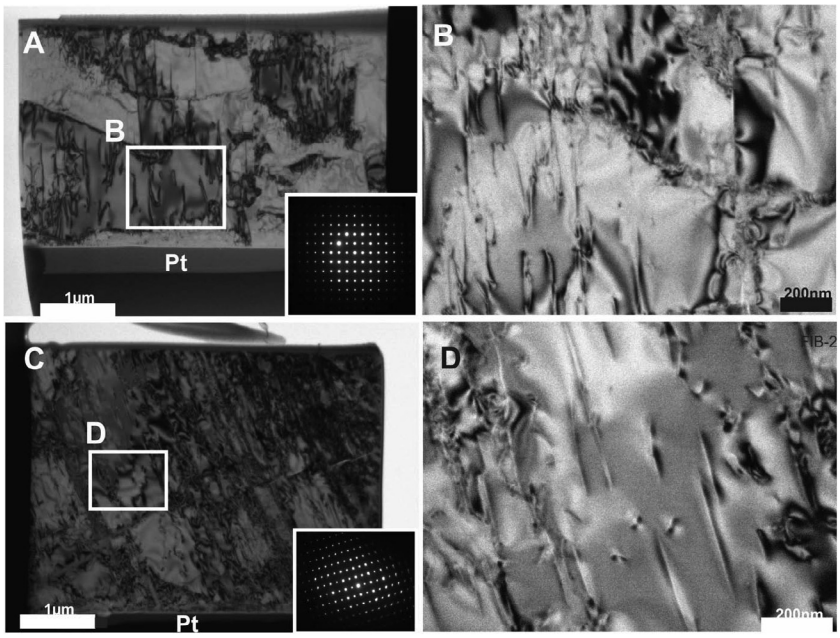

Fig. 4. Bright-field TEM images of FIB-1 (A,B) and FIB-2 (C,D). In A the inset [1 0 0] SAED pattern shows that the polished grain surface, on which the platinum (Pt) has been deposited, is parallel to the trace of (0 0 1). The dislocations lie parallel to the traces of (0 2 0) and [0 0 1], indicating that they are screw dislocations with a [0 0 1] Burgers vector on the (0 1 0) glide plane; such defects are typical of olivine deformed at high strain rate. The prominent subgrain boundary on the left hand side of the sample is parallel to the trace of (0 4 $\bar{1}$). The olivine in C and D also has a high dislocation density, and the inset [$\bar{1}$ 1 0] SAED pattern shows that these defects also lie parallel to [0 0 1].

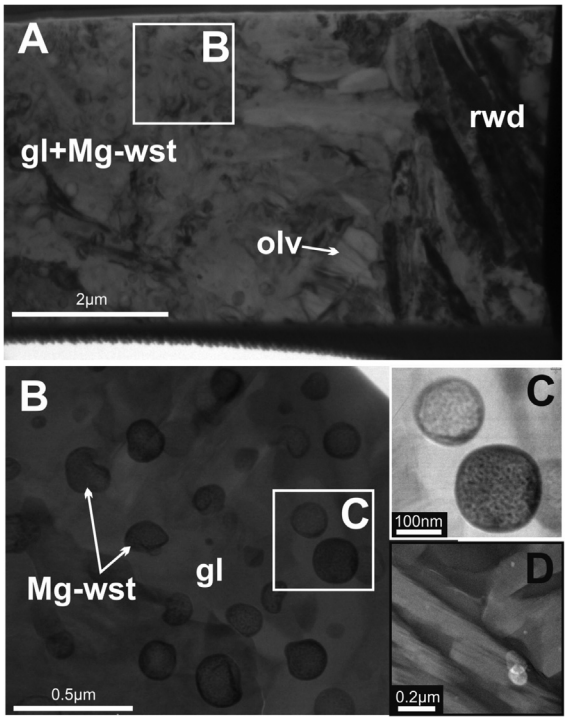

Fig. 5. Bright-field TEM images (A, C) bright-field STEM image (B) and HAADF STEM image (D) of FIB-section 3. The image of the whole section (A) shows numerous ringwoodite sub-grains nearest to the boundary with the olivine phenocryst (to the right), grading into a mixture of glass and magnesiowüstite spherules (B, C). Ringwoodite sub-grains show a typical fibrous texture (D).

if a proportion of the oxide spherules present are magnetite or a similar Fe-oxide. Although no magnetite was identified in FIB-3, Raman spectra do suggest the presence of magnetite rather than magnesiowüstite in numerous places within the sample (Fig. 2). The formation of magnesiowüstite and magnetite oxides explains the non-stoichiometry of ringwoodite, as this creates Mg and Fe vacancies in the ringwoodite structure. Ringwoodite can thus incorporate up to weight percent concentrations of hydroxyl, with charge compensated mainly by the Mg or Fe vacancies ($Mg/Fe^{2+} = 2H^{+}$), but also possibly as $Si^{4+} = 4H^{+}$ and $Mg/Fe^{2+} + 2H^{+} = Si^{4+}$ (Ye et al., 2012; Panero et al., 2013).

4. DISCUSSION

4.1. The shock history of Tissint

In combination, optical-microscope observations of plagioclase maskelynisation, shock blackening, strong olivine mosaicism and planar fracturing indicate the bulk of the Tissint meteorite was affected by an equilibration shock pressure of 35–40 GPa (Stöffler et al., 1991) (Fig. 7), with localised regions of "whole rock" melting (melt veins and pockets) requiring pressure excursions of up to 60 GPa. The occurrence of several high pressure phases in or near melt pockets (Baziotis et al., 2013; Summerson et al., 2013) supports these estimates. Based on Raman spectroscopy and TEM analysis of FIB-sections, Walton et al. (2014) concluded that the shock pressures experienced by Tissint were ⩾29–30 GPa. Our data agree with these pressure values. Therefore, the degree of shock shown by Tissint is higher in magnitude than that of Shergotty but lower than ALH 77005 (Fig. 7). It should be emphasized that the pressure values given above are derived from laboratory shock experiments performed at pre-impact temperatures of ~279 Kelvin. On Mars we expect distinctly lower pre-impact temperatures for small craters from which Martian meteorites are ejected. This would lead to even higher shock pressures for all shock effects discussed above, including those for melting (e.g., Langenhorst et al., 1992).

The dislocation densities in FIB-sections 1 and 2 indicate that olivine experienced shock pressures of 35–40 GPa, in line with olivine observed in shock stage 5 chondrites of Stöffler et al. (1991) and roughly similar to the 25–45 GPa range proposed for the Tenham L6 (S4) chondrite (Langenhorst et al., 1995).

Walton et al. (2014) suggest the thinnest shock veins (~20 μm) quench at the peak shock pressure within 10 ms, thus preserving high temperature/pressure minerals

Table 2
FIB-section 3 major and minor element mineral compositions.

Mineral	O	Mg	Si	Fe	Mn	Ca	Al	Total	Mg#	(Fe + Mg)/Si
Olv 1	39.08	23.97	18.42	18.14	0.38			99.99	98	2.01
Ringwoodite 1	37.69	30.24	23.07	9.01				100.01	89	1.71
Ringwoodite 2	37.1	26.01	21.78	15.11				100	80	1.73
Ringwoodite 3	38.74	29.95	21.31	9.99				99.99	87	1.86
Ringwoodite 4	37.71	30.23	23.06	9.01				100.01	89	1.71
Ringwoodite 5	39.14	25.88	25.94	8.23		0.81		100	88	1.36
Ringwoodite 6	38.09	30.01	24.14	7.76				100	90	1.60
Ringwoodite 7	38.8	27.74	25.76	7.7				100	89	1.39
Ringwoodite 8	39.12	29.46	26.23	5.19				100	93	1.40
Mg-wüstite 1	37.6	30.74	12.48	18.89	0.29			100	79	
Mg-wüstite 2	36.71	41.55	7.87	13.63			0.24	100	88	
Mg-wüstite 3	36.05	40.32	4.86	18.77				100	83	
Mg-wüstite 4	36.34	32.5	9.52	20.66	0.65		0.34	100.01	78	
Mg-wüstite 5	38.49	25.96	13.95	20.89	0.36		0.35	100	74	

Mg# = (Mg/(Fe + Mg)) * 100.
For stoichiometric olivine/ringwoodite (Fe + Mg)/Si = 2.00.

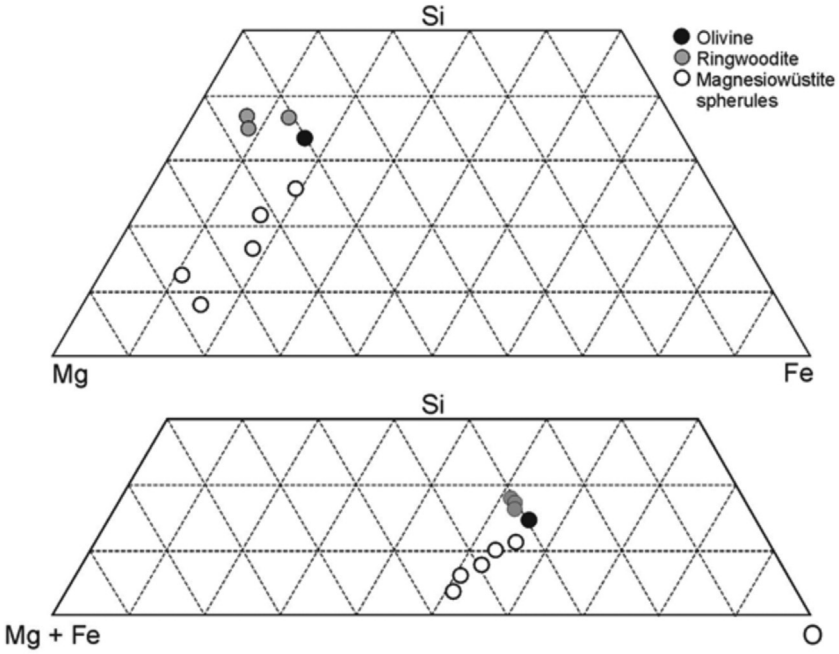

Fig. 6. Chemical compositions of olivine, ringwoodite and the magnesiowüstite spherules determined by STEM-EDX. Values are expressed as atomic %. The scatter in spherule analyses reflect variable mixing within the analysed volume between magnesiowüstite and ringwoodite/olivine. The data suggest that spherules uncontaminated by ringwoodite or olivine would have a composition of $\sim Mg_{0.9}Fe_{0.1}O$.

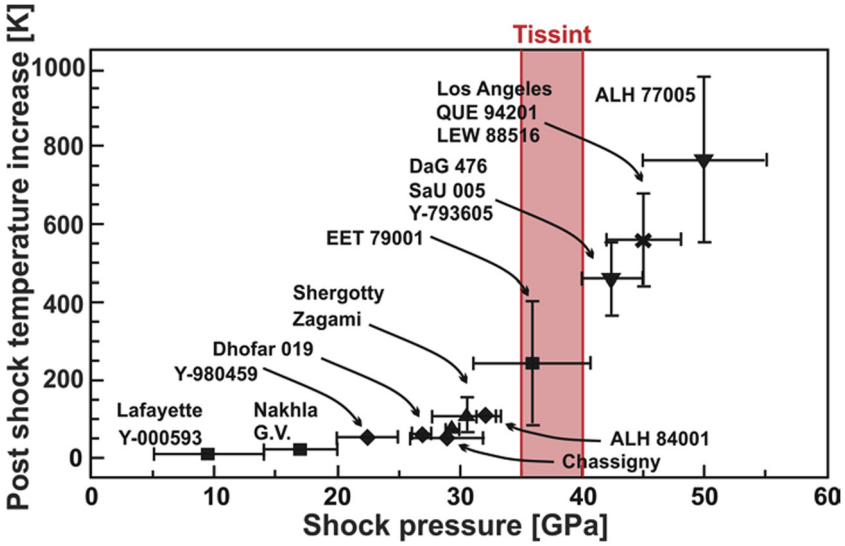

Fig. 7. Plot of shock temperature vs. pressure for a number of Martian meteorites. Estimates for Tissint pressures are shown by the shaded envelope, ranging from 35 to 40 GPa, with localised excursions of 45–50 GPa. Plot based on Fritz et al. (2005).

such as ringwoodite and stishovite. In contrast, thicker shock veins and melt pockets quench during pressure release (within 20–50 ms), or, in the case of the largest shock melt pockets/veins (>1 mm thick), quench occurs after decompression (within 1 s). Thus, lower temperature/-pressure phases, such as recrystallised clinopyroxene and olivine, as well as melt glass, are observed in these areas (Walton et al., 2014). The presence of ringwoodite and magnesiowüstite in the 100–200 μm thick BM.2012,M3_1 melt pocket is consistent with the previously observed mineralogies of thin/intermediate thickness shock veins, excepting the absence of silicate perovskite or clinopyroxene (e.g., Hu et al., 2013; Sharp et al., 2014; Walton et al., 2014). Calcium was detected for one EDX analysis of a ringwoodite

area in FIB-section 3 (Table 2), but neither SAED nor Raman spectroscopy results from the melt pocket revealed the presence of (Ca-bearing) silicate perovskite or clinopyroxene.

4.2. The relationship between shock pressure and hydrogen content in Martian minerals

The atmosphere of Mars has a δD value of ~4200‰, and so is much more highly enriched in deuterium than the Earth's atmosphere (Bjoraker et al., 1989; Webster et al., 2013). Therefore, high δD values in Tissint minerals suggest implantation of Martian atmospheric hydrogen, either from direct atmospheric implantation, or via interactions with atmosphere-equilibrated groundwater/ice.

Our Tissint measurements show that the highest δD values occur in recrystallized, shock-produced phases (ringwoodite and melt glass), indicating hydrogen in these phases is implanted from the Martian atmosphere during recrystallisation. This is in agreement with previous reports of highly elevated D/H ratios in Tissint shock melt pockets and some areas of maskelynite (Tucker et al., 2015; Chen et al., 2015; Mane et al., 2016). Based on elevated H_2O, F, Cl and CO_2 contents in shock melt pockets, Chen et al. (2015) suggested that Tissint interacted with aqueous-alteration products after its parental melt erupted. These authors argued that the Martian atmosphere cannot be the sole contributor to Tissint's elevated NOM D/H ratio and water content, because of the high abundances of H_2O, F, and Cl relative to CO_2 in impact melt pockets, which is the opposite trend to that seen in the current Martian atmosphere (Mahaffy et al., 2013). However, Tissint is a depleted shergottite from a parental melt that shows no evidence of crustal assimilation prior to or during crystallization (Balta et al., 2015), hence any interaction could only have been with relatively pure F and Cl-rich fluid – e.g., groundwater. This interaction must have occurred prior to crystallisation, as Tissint contains no mineralogical evidence for Martian aqueous alteration. In this case, all minerals in Tissint should exhibit the groundwater chemical signature, including elevated δD values. Hence, the low δD values exhibited by olivine and some maskelynite areas (Tucker et al., 2015; Mane et al., 2016) argue against Martian groundwater interaction with Tissint.

Olivine in Tissint does show signs of shock (<35 GPa based on dislocation densities), but contains water with low δD values compared to ringwoodite and melt glass; ⩽88‰ (our data), ⩽470‰ (Mane et al., 2016). In addition, direct comparison of water contents in BM.2012,M3_1 reveals elevated abundances in ringwoodite (714–1132 ppm H_2O) compared to olivine (230–485 ppm H_2O). Therefore, it appears that recrystallization greatly aids atmospheric hydrogen implantation in olivine.

High δD values have been previously reported from primary hydrous minerals in other shergottites. For example, Watson et al. (1994) recorded δD values of +512 to +1672‰ in amphiboles from Shergotty and Zagami. Apatites in these two meteorites yield even higher δD values (+2953 to +4606‰ in Shergotty and +2962 to +4358‰ in Zagami, Watson et al., 1994; Greenwood et al., 2008; Hallis et al., 2012b). More recently, GRV 020090 apatite and melt inclusion δD values between +737 and +5337‰ have been reported (Hu et al., 2014). Atmospheric hydrogen implantation via high shock pressures could explain these high δD values (Bogard et al., 1986, 1989; Wiens and Pepin, 1988; Minitti et al., 2007, 2008), but it is worth noting that Shergotty, Zagami and GRV 020090 are enriched shergottites with much younger crystallisation ages than Tissint (e.g., Nyquist et al., 2001). Enriched shergottites have slightly higher water contents (e.g., McCubbin et al., 2016), suggesting open system crystallisation involving the addition of a REE/water-enriched component (Herd et al., 2002). In addition, Zagami has been reported to contain a crustal component (Franz et al., 2014; Williams et al., 2016). As Martian crustal material is expected to have high δD values because of equilibration with Martian atmospheric hydrogen, the addition of crustal water to the Zagami melt could have (at least partially) raised the δD to current values, especially in late crystallising apatite.

4.3. The source of water in Tissint olivine

Sample P18494 is epoxy mounted, and so cannot be relied upon to yield correct water contents for the analysed minerals or glasses. However, careful preparation of sample BM.2012,M3_1, which was mounted in indium without the use of water during polishing, and was subsequently stored in a vacuum oven, means it is as free of terrestrial water as possible. Therefore, the following discussion is based on the water content of olivine only in sample BM.2012,M3_1, as well as previously published data. Tissint olivine contains detectable and variable H_2O, as also shown by Mane et al. (2016). Olivine has a low D/H ratio (δD ⩽ 470‰, Mane et al., 2016), meaning the majority of water was not implanted from the Martian atmosphere, as appears to be the case for ringwoodite and shock melt pockets in Tissint. Three sources of low-δD water should be considered for Tissint olivine: 1. Terrestrial water contamination, 2. Martian primary water inherited by olivine from the parental melt, or 3. Martian post-magmatic processing involving a water reservoir with low D/H ratio.

4.3.1. Terrestrial contamination?

Although Tissint was collected soon after it fell, terrestrial atmospheric water may have been adsorbed into minerals via dislocations. This adsorption would explain the low δD values measured in olivine. However, previously reported water contents of olivine in the shergottite meteorites EETA 79001 (lithology B) and ALH 77005 are much lower than those measured in Tissint: 29 ± 3 ppm and 0.53 ± 0.12 ppm, respectively (Boctor et al., 2003), compared to 642–1354 ppm in BM.2012,M3_1. This difference is all the more notable because ALH 77005 and EETA 79001 were both found in Antarctica, and so had considerable terrestrial exposure. Olivine within the Martian meteorites Chassigny and Shergotty, both of which were seen to fall in the 19th century, also has low water contents (88 ± 11 ppm and 12–86 ppm, respectively; Boctor et al., 2003; Hallis et al., 2012b). EETA 79001 and ALH 77005 show evidence for

levels of shock equal to and above (in the case of the latter) Tissint (Fig. 7), and so their olivine grains would be expected to have comparable or greater densities of dislocations, which could facilitate the ingress of terrestrial water. Therefore, it seems unlikely that Tissint olivine would have adsorbed so much water from the terrestrial atmosphere when olivines in other similar meteorites have not.

4.3.2. Parental-melt water in olivine?

If the high water content of Tissint olivine cannot be explained by terrestrial contamination, it may have originated in the parental melt. Different studies suggest the shergottite source regions are water-poor (e.g., Patiño-Douce and Roden, 2006; Jones, 2015; McCubbin et al., 2016), slightly water-poor (Gross et al., 2013), or contain similar water contents compared to the terrestrial mantle (e.g., McCubbin et al., 2012). This suggests shergottite olivine should have similar or lower water contents to those in terrestrial basalts such as the MORB lavas (<200 ppm, Manghnani et al., 2013). However, Martian mantle olivine is Fe-rich compared to that of the terrestrial mantle ($Fo_{67–81}$ vs. $Fo_{89.5}$, respectively, Withers et al., 2011 and references therein), and Fe-rich olivine can retain more H_2O than Mg-rich olivine (Zhao et al., 2004; Withers et al., 2011). Tissint macrocrysts and phenocrysts have core compositions of $Fo_{80–81}$ and $Fo_{70–77}$, respectively (Hsu et al., 2012; Irving et al., 2012). Hence, Tissint olivine could retain more water than MORB olivine from a parental melt with the same H_2O abundance. Withers et al. (2011) reported that, at pressures of 3–6 GPa, olivine with compositions corresponding to the Martian mantle could retain a maximum of 300–400 ppm H_2O. These values are comparable to Tissint olivine water contents, but the pressure range is much higher than the pressure of Tissint olivine formation. Olivine macrocrysts in Tissint probably crystallised at depths comparable with olivine macrocrysts in Yamato 980459 – another depleted olivine-phyric shergottite representing a primitive Martian melt (Musselwhite et al., 2006). Yamato 980459 macrocrysts have an estimated equilibration pressure/temperature of 1.7 GPa/1550 °C (Lee et al., 2009). Therefore, even the deepest crystallised olivine in Tissint was not formed at pressures great enough to produce H_2O contents higher than MORB olivine (<200 ppm, Manghnani et al., 2013). In addition, not all olivine in Tissint formed at depth. The shergottites are reported to have finished crystallisation at relatively low pressures, within a few hundred metres of the Martian surface (e.g., Greshake et al., 2004; Beck et al., 2005). Therefore, Tissints late-crystallising olivine phenocrysts formed at low pressure. It is worth noting here that both olivine macrocryst and phenocryst water contents were measured in sample P18494, with no visible distinction between the two populations (Fig. 3). Based on the above evidence it seems improbable that the high water content in Tissint olivine is a direct product of high parental melt water content.

4.3.3. Crustal contamination?

The shergottites show no petrographic indications of olivine alteration, such as that exhibited in the nakhlites (e.g., Lee et al., 2015). However, Tissint has been reported to contain water-rich amphibole within early-crystallised pigeonite, indicating a parental-melt H_2O abundance of 2500–5600 ppm (Williams et al., 2014). This is much higher than recent estimates of depleted shergottite parental melt H_2O compositions (139–186 ppm), based on samples with no evidence of crustal contamination (Usui et al., 2012; McCubbin et al., 2016). Therefore, the presence of amphibole in pigeonite may indicate the addition of crustal groundwater/ice to the Tissint parental melt prior to crystallisation. In addition, merrillite in Tissint contains intermediate δD values (+272 to +2418‰) and relatively high water contents (400–2200 ppm H_2O), which Mane et al. (2016) report as the result of partial equilibration with aqueous fluids derived from a distinct Martian reservoir comprised of hydrated crust or ground ice, as proposed by Usui et al. (2015).

Usui et al. (2015) argue that the variable δD values of shergottite shock-induced melt glasses, as well as bulk rock δD from shergottites, nakhlites and ALH 84001, suggest the presence of a third water reservoir on Mars, with δD values of ~1000–2000‰ – lower than the δD of the Martian atmosphere but higher than that of the Martian interior. This water reservoir is suggested to represent hydrated crust and/or ground ice interbedded within sediments. However, the olivine δD values measured for this and previous studies (Mane et al., 2016) are much lower than 1000‰ (−149 to 470‰), suggesting either partial equilibration with this crustal fluid, or that another source of water caused olivine hydration in Tissint.

4.3.4. Post-magmatic processing?

Deuteric alteration may provide a way to explain the low δD and high water contents of Tissint's olivine, as suggested by Tucker et al. (2015) based on similar properties in Tissint maskelynite. This type of alteration takes place during the final crystallisation stages of molten rock, and is caused by residual water-rich vapour or fluid permeating along crystal boundaries and fractures. Extensive deuteric alteration of olivine commonly produces chlorite or iddingsite (Baker and Haggerty, 1967; Delvigne et al., 1979). Optical microscopy, Raman spectra and TEM SAED patterns give no indication that olivine has been altered to these minerals in Tissint, but it may be that insufficient water was available for deuteric alteration to progress beyond the initial stages in Tissint. The presence of magnetite in Tissint has been reported as a deuteric alteration product of ulvöspinel (Gattacceca et al., 2013).

The residual vapour/fluid that causes this type of alteration is sourced from the melt itself, which should have a low δD value similar to those measured in Martian primary hydrous phases unaffected by atmospheric hydrogen (<275‰, Usui et al., 2012; Hallis et al., 2012b). However, the shergottites are likely to have undergone significant degassing during crystallisation (e.g., McCubbin et al., 2012, 2016), and this could have changed the D/H ratio of the melt. Tissint crystallised under reducing conditions (e.g., Balta et al., 2015), hence dehydrogenation (loss of H_2) would have been the dominant mechanism for degassing. Dehydrogenation would thus have resulted in D/H ratio elevation in the Tissint residual melt compared to

the parental melt (Tartèse and Anand, 2013), possibly explaining slightly elevated δD values in olivine compared to proposed Martian mantle values; ⩽470‰ vs. <275‰ (Usui et al., 2012; Mane et al., 2016, respectively). Based on our data, deuteric alteration during late-stage crystallisation, the addition of groundwater/ice with low D/H ratios prior to crystallisation, or a combination of both, are the most probable explanations for the presence of water in Tissint olivine.

5. CONCLUSIONS

The Tissint Martian meteorite contains minerals and shock melts produced by pressures of 35–40 GPa, with evidence of excursions up to 45–60 GPa. Mixtures of shock-produced ringwoodite, magnesiowüstite and magnetite exhibit high δD values (3834–4224‰), indicative of the implantation of Martian atmospheric hydrogen during shock recrystallization. Although olivine in Tissint has been shocked (35–40 GPa), only recrystallised and shock-melted areas of the meteorite (45–60 GPa) contain the very high δD values (>1000‰) associated with atmospheric hydrogen implantation.

Tissint olivine exhibits detectable water contents with low δD values. The addition of groundwater/ice with low D/H ratios prior to crystallisation, deuteric alteration during late-stage crystallisation, or a combination of both, could explain the presence of this water. Via these processes low D/H ratio fluids could have been incorporated into Tissint nominally anhydrous minerals, such as olivine and maskelynite.

ACKNOWLEDGEMENTS

The research leading to these results has received funding from the People Programme (Marie Curie Actions) of the European Union's Seventh Framework Programme (FP7/2007-2013) under REA grant agreement No. 624137. This research was partially supported by the National Aeronautics and Space Administration through the NASA Astrobiology Institute under Cooperative Agreement No. NNA09-DA77A, issued through the Office of Space Science. We also acknowledge funding from the UK STFC through grants ST/H002960/1, ST/K000942/1 and ST/L002167/1. Billy Smith, Colin How and Sam MacFadzean are thanked for their help with the FIB and TEM, and we are grateful to the Natural History Museum (London) for loan of the Tissint samples. Associate Editor Prof. Gregory Herzog, along with Dr. Tomohiro Usui and two anonymous reviewers are thanked for their helpful comments and suggestions.

APPENDIX A. SUPPLEMENTARY DATA

Supplementary data associated with this article can be found, in the online version, at http://dx.doi.org/10.1016/j.gca.2016.12.035.

REFERENCES

Aubaud C., Withers A. C., Hirschmann M. M., Guan Y., Leshin L. A., Mackwell S. J. and Bell D. R. (2007) Intercalibration of FTIR and SIMS for hydrogen measurements in glasses and nominally anhydrous minerals. *Am. Mineral.* **92**, 811–828.

Baker I. and Haggerty S. E. (1967) The alteration of olivine in basaltic and associated lavas part II: Intermediate and low temperature alteration. *Contr. Mineral. Petrol.* **16**, 258–273.

Balta J. B., Sanborn M. E., Udry A., Wadhwa M. and McSween H. Y. (2015) Petrology and trace element geochemistry of Tissint, the newest shergottite fall. *Meteorit. Planet. Sci.* **50**, 63–85.

Baziotis I. P., Liu Y., DeCarli P. S., Melosh H. J., McSween H. Y., Bodnar R. J. and Taylor L. A. (2013) The Tissint Martian meteorite as evidence for the largest impact excavation. *Nature Comm.* **4**, 1404. http://dx.doi.org/10.1038/ncomms2414.

Beck P., Gillet P., El Goresy A. and Mostefaoui S. (2005) Timescales of shock processes in chondritic and Martian meteorites. *Nature* **435**, 1071–1074.

Bjoraker G. L., Mumnya M. J. and Larson H. P. (1989) The value of D/H in the Martian atmosphere. *Bull. Am. Astron. Soc.* **21**, 990. Abstract.

Boctor N. Z., Alexander C. M. O'D., Wang J. and Hauri E. (2003) The sources of water in Martian meteorites: clues from hydrogen isotopes. *Geochim. Cosmochim. Acta* **67**, 3971–3989.

Bogard D. D., Hörz F. and Johnson P. H. (1986) Shock implanted noble gases: an experimental study with implications for the origin of Martian gases in shergottite meteorites. *J. Geophys. Res.* **91**, E99–E114.

Bogard D. D., Hörz F. and Johnson P. H. (1989) Shock implanted noble gases II: additional experimental studies and recognition in naturally shocked terrestrial materials. *Meteoritics* **24**, 113–123.

Borg L. E. et al. (2001) The age of Dhofar 019 and its relationship to the other Martian meteorites. *Lunar Planet. Sci.* **32**, 1144.

Brennecka G. A., Borg L. E. and Wadhwa M. (2014) *Insights into the Martian mantle: the age and isotopics of the meteorite fall Tissint*. Planet. Sci, Met, 10.1111/maps.12258.

Chen Y., Liu Y., Guan Y., Eiler J. M., Ma C., Rossman G. R. and Taylor L. A. (2015) Evidence in Tissint for recent subsurface water on Mars. *Earth Planet. Sci. Lett.* **425**, 55–63.

Chennaoui Aoudjehane H. et al. (2012) Tissint Martian meteorite: a fresh look at the interior, surface, and atmosphere of Mars. *Science* **338**, 785–788.

Delvigne J., Bisdom E. B. A., Sleeman J. and Stoops G. (1979) Olivines, their pseudomorphs and secondary products. *Pedologie XXIX* **3**, 247–309.

Donahue T. M. (1995) Evolution of water reservoirs on Mars from D/H ratios in the atmosphere and crust. *Nature* **374**, 432–434.

Franz H. B., Kim S. T., Farquhar J., Day J. M. D., Economos R. C., McKeegan K. D., Schmitt A. K., Irving A. J., Hoek J. and Dottin J. (2014) Isotopic links between atmospheric chemistry and the deep sulphur cycle on Mars. *Nature* **508**, 364–368.

Fritz J., Artemieva N. and Greshake A. (2005) Ejection of Martian meteorites. *Meteorit. Planet. Sci.* **40**(Nr 9/10), 1393–1411.

Gattacceca J. et al. (2013) Opaque minerals, magnetic properties, and paleomagnetism of the Tissint Martian meteorite. *Meteorit. Planet. Sci.* **48**, 1919–1936.

Giesting P. A., Schwenzer S. P., Filiberto J., Starkey N. A., Franchi I. A., Treiman A. H., Tindle A. G. and Grady M. M. (2015) Igneous and shock processes affecting chassignite amphibole evaluated using chlorine/water partitioning and hydrogen isotopes. *Meteorit. Planet. Sci.* **50**, 433–460.

Greenwood J. P., Itoh S., Sakamoto N., Vicenzi E. P. and Yurimoto H. (2008) Hydrogen isotope evidence for loss of water from Mars through time. *Geophys. Res. Lett.* **35**, L05203.

Greshake A., Fritz J. and Stöffler D. (2004) Petrology and shock metamorphism of the olivine-phyric Shergottite Yamato

980459: evidence for a two-stage cooling and single-stage ejection history. *Geochim. Cosmochim. Acta* **68**, 2359–2377.

Gross J., Filiberto J. and Bell A. S. (2013) Water in the Martian interior: Evidence for terrestrial MORB mantle like volatile contents from hydroxyl-rich apatite in olivine phyric shergottite NWA 6234. *Earth Planet. Sci. Lett.* **369**, 120–128.

Hallis L. J., Taylor G. J., Nagashima K., Huss G. R., Needham A. W., Franchi I. A. and Grady M. M. (2012a) Hydrogen isotope analyses of alteration phases in the nakhlite Martian meteorites. *Geochim. Cosmochim. Acta* **97**, 105–119.

Hallis L. J., Taylor G. J., Nagashimaa K. and Huss G. R. (2012b) Magmatic water in the Martian meteorite Nakhla. *Earth Planet. Sci. Lett.* **359–360**, 84–92.

Hauri E. H. (2002) SIMS analysis of volatiles in silicate glasses, 2: isotopes and abundances in Hawaiian melt inclusions. *Chem. Geol.* **183**, 115–141.

Hauri E. H., Shaw A. M., Wang J., Dixon J. E., King P. L. and Mandeville C. (2006) Matrix effects in hydrogen isotope analysis of silicate glasses by SIMS. *Chem. Geol.* **235**, 352–365.

Herd C. D. K., Borg L. E., Jones J. H. and Papike J. J. (2002) Oxygen fugacity and geochemical variations in the martian basalts: implications for martian basalt petrogenesis and the oxidation state of the upper mantle of Mars. *Geochim. Cosmochim. Acta* **66**, 2025–2036.

Hsu W., Wu Yunhua and Jiang Yun. (2012) Petrology and mineralogy of the Tissint olivine-phyric Shergottite. In *75th Annual Meteoritical Society Meeting #5080*.

Hu J., Sharp T. G. and Walton E. L. (2013) Shock effects in Tissint II: olivine transformation to silicate perovskite and oxide (abs). *Lunar Planet. Sci. Conf* **44**, 1041.

Hu S., Lin Y., Zhang J., Hao J., Feng L., Xu L., Yang W. and Yang J. (2014) NanoSIMS analyses of apatite and melt inclusions in the GRV 022090 Martian meteorite: hydrogen isotope evidence for recent past underground hydrothermal activity on Mars. *Geochim. Cosmochim. Acta.* **140**, 321–333.

Irving A. J., Kuehner S. M., Tanaka R., Herd C. D. K., Chen G. and Lapan T. J. (2012) The Tissint depleted permafic olivine-phyric Shergottite: petrologic, elemental and isotopic characterization of a recent Martian Fall in Morocco. *Lunar Planet. Sci. Conf.* **43**, 2510.

Jones J. H. (2015) Various aspects of the petrogenesis of the Martian shergottite meteorites. *Met. Planet. Sci.* **50**, 674–690.

Koch-Muller M., Rhede D., Schulz R. and Wirth R. (2009) Breakdown of hydrous ringwoodite to pyroxene and spinelloid at high P and T and oxidizing conditions. *Phys. Chem. Minerals* **36**, 329–341.

Langenhorst F., Deutsch A., Stöffler D. and Hornemann U. (1992) Effect of temperature on shock metamorphism of single-crystal quartz. *Nature* **356**, 507–509.

Langenhorst F., Joreau P. and Doukhan J. C. (1995) Thermal and shock metamorphism of the Tenham chondrite: a TEM examination. *Geochim. Cosmochim. Acta* **59**, 1835–1845.

Lee M. R., Bland P. A. and Graham G. (2003) Preparation of TEM samples by focused ion beam (FIB) techniques: applications to the study of clays and phyllosilicates in meteorites. *Mineral. Mag.* **67**, 581–592.

Lee C.-T. A., Luffi P., Plank T., Dalton H. and Leeman W. P. (2009) Constraints on the depths and temperatures of basaltic magma generation on Earth and other terrestrial planets using new thermobarometers for mafic magmas. *Earth Planet. Sci. Lett.* **279**, 20–33.

Lee M. R., Tomkinson T., Hallis L. J. and Mark D. F. (2015) Formation of iddingsite veins in the Martian crust by centripetal replacement of olivine: evidence from the nakhlite meteorite Lafayette. *Geochim. Cosmochim. Acta* **154**, 49–65.

Ma C., Tschauner O., Beckett J. R., Liu Y., Rossman G. R., Zuravlev K., Prakapenka V., Dera P. and Taylor L. A. (2015) Tissintite (Ca, Na)$AlSi_2O_6$: a highly-defective, shock-induced, high-pressure clinopyroxene in the Tissint Martian meteorite. *Earth Planet. Sci. Lett.* **422**, 194–205.

Mahaffy P. R. et al. (2013) Abundance and isotopic composition of gases in the Martian atmosphere from the Curiosity Rover. *Science* **341**, 263–266.

Mane P., Hervig R., Wadhwa M., Garvie L. A. J., Balta J. B. and McSween, Jr., H. Y. (2016) *Hydrogen isotopic composition of the Martian mantle inferred from the newest Martian meteorite fall*. Meteorit. Planet. Sci, Tissint, 10.1111/maps.12717.

Manghnani M. H., Hushuri A., Smyth J. R., Nestola F., Dera P., Sekar M., Amulele G. and Frost D. J. (2013) Compressibility and structural stability of two variably hydrated olivine samples ($Fo_{97}Fa_3$) to 34 GPa by X-ray diffraction and Raman spectroscopy. *Am. Mineralogist* **98**, 1972–1979.

Marquardt H., Speziale S., Reichmann H. J., Frost D. J., Schilling F. R. and Garnero E. J. (2009) Elastic shear anisotropy of ferropericlase in Earth's lower mantle. *Science* **324**, 224–226.

McCubbin F. M., Hauri E. H., Elardo S. M., Vander Kaaden K. E., Wang J. and Shearer C. K. (2012) Hydrous melting of the Martian mantle produced both depleted and enriched shergottites. *Geology* **40**, 683–686.

McCubbin F. M., Boyce J. W., Srinivasan P., Santos A. R., Elardo S. M., Filiberto J., Steele A. and Shearer C. K. (2016) Heterogeneous distribution of H_2O in the Martian interior: implications for the abundance of H_2O in depleted and enriched mantle sources. *Met. Planet. Sci.*. http://dx.doi.org/10.1111/maps.12639.

Minitti M. E., Rutherford M. J., Taylor B. E., Dyar M. D. and Schultz P. H. (2007) Assessment of shock effects on amphibole water contents and hydrogen isotope compositions: 1. Amphibolite experiments. *Earth Planet. Sci. Lett.* **266**, 46–60.

Minitti M. E., Leshin L. A., Dyar M. D., Ahrens T. J., Guan Y. and Luo S.-N. (2008) Assessment of shock effects on amphibole water contents and hydrogen isotope compositions: 2. Kaersutitic amphibole experiments. *Earth Planet. Sci. Lett.* **266**, 288–302.

Mosenfelder J. L., Le Voyer M., Rossman G. R., Guan Y., Bell D. R., Asimow P. D. and Eiler J. M. (2011) Analysis of hydrogen in olivine by SIMS: evaluation of standards and protocol. *Am. Mineral.* **96**, 1725–1741.

Musselwhite D. S., Dalton H. A., Kiefer W. S. and Treiman A. H. (2006) Experimental petrology of the basaltic Shergottite Yamato-980459: implications for the thermal structure of the Martian mantle. *Met. Planet. Sci.* **41**, 1271–1290.

Nishiizumi K., Caffee M. W. and Irving A. J. (2012) Exposure history of Tissint: evidence for 1.1 million year launch pairing with other depleted olivine-phyric Shergottites. *Meteorit. Soc.* **75**, 5349.

Nyquist L. E., Bogard D. D., Shih C., Greshake A., Stöffler D. and Eugster O. (2001) Ages and geologic histories of Martian meteorites. *Space Sci. Rev.* **96**, 105–164.

Panero W. R., Smyth J. R., Pigott J. S., Liu Z. and Frost D. J. (2013) Hydrous ringwoodite to 5 K and 35 GPa: multiple hydrogen bonding sites resolved with FTIR spectroscopy. *Am. Mineral.* **98**, 637–642.

Patiño-Douce A. E. and Roden M. F. (2006) Apatite as a probe of halogen and water fugacities in the terrestrial planets. *Geochim. Cosmochim. Acta* **70**, 3173–3196.

Sharp T. G., Walton E. L. and Hu J. (2014) Shock effects in Tissint: evidence against a long duration shock and large impacting body (abs). *Lunar Planet. Sci. Conf.* **45**, 2820.

Shaw A. M., Hauri E. H., Behn M. D., Hilton D. R., Macpherson C. G. and Sinton J. M. (2012) Long-term preservation of slab

signatures in the mantle inferred from hydrogen isotopes. *Nature Geo.* **5**, 224–228.

Smith C. L. and Ahmed F. (2012) X-ray microtomography of the Tissint Martian meteorite.In *75th Ann. Met. Soc. Meeting.* #5138.

Stöffler D., Keil K. and Scott E. R. D. (1991) Shock metamorphism of ordinary chondrites. *Geochim. Cosmochim. Acta* **55**, 3845–3867.

Summerson I., Greshake A., Fritz J. and Reimold U. (2013) High-pressure phases in a melt pocket within olivine macrocryst in the Tissint Martian meteorite. *Lunar Planet. Sci. Conf.* **44**, 1974.

Tartèse R. and Anand M. (2013) Late delivery of chondritic hydrogen into the lunar mantle: Insights from mare basalts. *Earth Planet. Sci. Lett.* **361**, 480–486.

Tucker K., Hervig R. and Wadhwa M. (2015) Hydrogen isotope systematics of nominally anhydrous phases in Martian meteorites (abs). *Lunar Planet. Sci. Conf.* **46**, 2915.

Tyburczy J. A., Krishnamurthy R. V., Epstein S. and Ahrens T. J. (1990) Impact-induced devolatilization and hydrogen isotopic fractionation of serpentine: implications for planetary accretion. *Earth Planet. Sci. Lett.* **98**, 245–261.

Tyburczy J. A., Xu X., Ahrens T. J. and Epstein S. (2001) Shock-induced devolatilization and isotopic fractionation of H and C from Murchison meteorite: some implications for planetary accretion. *Earth Planet. Sci. Lett.* **192**, 23–30.

Usui T., Alexander C. M. O'D., Wang J., Simon J. I. and Jones J. H. (2012) Origin of water and mantle–crust interactions on Mars inferred from hydrogen isotopes and volatile element abundances of olivine-hosted melt inclusions of primitive shergottites. *Earth Planet. Sci. Lett.* **357–358**, 119–129.

Usui T., Alexander C. M. O'D., Wang J., Simon J. I. and Jones J. H. (2015) Meteoritic evidence for a previously unrecognized hydrogen reservoir on Mars. *Earth Planet. Sci. Lett.* **410**, 140–151.

Walsh S. R., Rusakova I. and Whitmire K. H. (2013) Rock salt vs. wurtzite phases of $Co_{1-x}Mn_xO$: control of crystal lattice and morphology at the nanoscale. *Cryst. Eng. Commun.* **15**, 775.

Walton E. L., Sharp T. G., Hu J. and Filiberto J. (2014) Heterogeneous mineral assemblages in Martian meteorite Tissint as a result of a recent small impact event on Mars. *Geochim. Cosmochim. Acta* **140**, 334–348.

Watson L., Hutcheon I. D., Epstein S. and Stolper E. M. (1994) Water on Mars: clues from deuterium/hydrogen and water contents of hydrous phases in SNC meteorites. *Science* **265**, 86–90.

Webster C. R. et al. (2013) Isotope ratios of H, C, and O in CO_2 and H_2O of the Martian atmosphere. *Science* **341**, 260–263.

Wiens R. C. and Pepin R. O. (1988) Laboratory shock emplacement of noble gases, nitrogen, and carbon dioxide into basalt, and implications for trapped gases in shergottite EETA 79001. *Geochim. Cosmochim. Acta* **52**, 295–307.

Williams K. B., Sonzogni Y. and Treiman A. H. (2014) Amphibole in the Tissint Martian meteorite: composition and implication for volatile content of parental magma. *Lunar Planet. Sci. Conf.* **45**, 1435.

Williams J. T., Shearer, Jr., C. K., Sharp Z. D., Burger P. V., McCubbin F. M., Santos A. R., Agee C. B. and McKeegan K. D. (2016) The chlorine isotopic composition of Martian meteorites 1. Chlorine isotopic composition of the Martian mantle, crustal, and atmospheric reservoirs and their interactions. *Met. Planet. Sci.* **51**, 2092–2110.

Withers A. C., Hirschmann M. M. and Tenner T. J. (2011) The effect of Fe on olivine H_2O storage capacity: consequences for H_2O in the martian mantle. *Am. Mineral.* **96**, 1039–1053.

Xia Z., Sharp T. G. and DeCarli P. S. (2006) High-pressure phases in a shock-induced melt vein of the Tenham L6 chondrite: constraints on shock pressure and duration. *Geochim. Cosmochim. Acta* **70**, 504–515.

Ye Y. et al. (2012) Compressibility and thermal expansion of hydrous ringwoodite with 2.5(3) wt % H_2O. *Am. Mineral.* **97**, 573–582.

Zhao Y.-H., Ginsberg S. B. and Kohlstedt D. L. (2004) Solubility of hydrogen in olivine: dependence on temperature and iron content. *Contrib. Mineral. Petrol.* **147**, 155–161.

Associate editor: Gregory F. Herzog